Discovering and Dissecting Mechanically Excited Luminescence of Mn^{2+} Activators *via* Matrix Microstructure Evolution

Jun-Cheng Zhang, Nan Gao, Lei Li, Shanshan Wang, Xiaofeng Shi, Mingzi Sun, Xu Yan, Hong-Wei He, Xin Ning, Bolong Huang,* and Jianrong Qiu*

Prof. J.-C. Zhang, Dr. S. Wang, Dr. X. Shi
Department of Physics

College of Information Science and Engineering

Ocean University of China

Qingdao 266100, China

E-mail: zhangjuncheng@ouc.edu.cn

N. Gao, L. Li
College of Physics
Qingdao University
Qingdao 266071, China

Dr. X. Yan, Dr. H.-W. He, Prof. X. Ning
Industrial Research Institute of Nonwovens & Technical Textiles
Qingdao University
Qingdao, 266071, China

Prof. B. Huang, M. Sun

Department of Applied Biology and Chemical Technology

The Hong Kong Polytechnic University

Hong Kong SAR, China

E-mail: bhuang@polyu.edu.hk

Prof. J. Qiu
State Key Laboratory of Modern Optical Instrumentation
Zhejiang University
Hangzhou 310027, China

Keywords: mechanoluminescence; piezoluminescence; triboluminescence; crystal structure; electronic structure

Mechanoluminescent (ML) materials featuring renewable mechanical-to-optical conversion have shown promising prospects in stress sensing, lighting and display. However, the advancement in ML applications is being restrained by the obstacles in developing efficient ML materials and understanding the underlying ML mechanisms. Herein, a matrix evolution strategy to modulate the local microstructure and electronic environment around the luminescent activators is proposed, which not only supports the batch development of new ML materials but also provides a well-connected platform for systematically revealing the mechanism of achieving efficient ML performance. The feasibility of the strategy has been proved by constructing and evaluating a series of ML materials with matrix-dependent luminescent properties in experimental-theoretical collaboration. It has been demonstrated that the construction of piezoluminescence is available in both non-centrosymmetric and centrosymmetric matrices, without being restricted by lattice symmetry. The inter-electronic-levels and shallow electron traps formed by activator doping enhance the electron recombination efficiency through both tunneling and conduction band transfer pathways. Our results are expected to accelerate the exploitation of ML material systems and to deepen the comprehensive apprehending of ML mechanisms, thereby guiding the rational design and widespread use of efficient ML materials.

1. Introduction

The mechanical stimulations caused by Newtonian forces are extremely universal physical actions, widely distributed in human activities related to the conversion and harvest of mechanical energy. The detection and utilization of mechanical stimulation have ever been

extensively concerned due to the intriguing physics and widespread applications.[1-9] Among many emerging technologies, recoverable mechanoluminescence (ML) with a marvelous mechanically excited luminescence exhibits the outstanding advantages of quantitative mechanical-to-optical conversion and renewable light emission under cyclic mechanical stimuli. Such an advanced technology has shown potential applications in many fields including stress sensing, displays, lighting, bio-imaging, anti-counterfeiting, and wearable devices.[10-25]

To promote these attractive potentials of recoverable ML to practical applications, it is essential to expand the quantity of efficient ML materials and ascertain the underlying ML mechanisms. Over the past 20 years, increasing attention has been focused on the development of ML materials with different characteristics including intense brightness, high mechanical sensitivity, abundant emission wavelengths, excellent luminous reproducibility, as well as physical and chemical stability.[26-36] Despite the significant effort made, there are only dozens of recoverable ML materials known to date, of which a few show high ML performance.[37] The main reason for the lagging development of ML materials is the discovery-based approach rather than the rational design strategy. For example, most recoverable ML materials belong to the type of trap-controlled piezoluminescence (so-called piezoelectric ML), in which the ML is generated by releasing the captured carriers under the piezoelectric field and then recombining carriers in the luminescent centers. Therefore, the discovery-based approach mainly adopts two schemes, namely screening persistent phosphors with non-centrosymmetric structures and doping luminescent activators in piezoelectric matrices.[38-43] However, these two schemes are still far from the inverse design-based approach to obtain the required performance of ML materials. Moreover, the former one is limited by the available candidates of persistent phosphors with piezoelectricity while the latter one regularly suffers from the luminescence quenching of

activators in piezoelectric. On the other hand, previous fundamental research on ML materials generally focuses on the individual phenomena of isolated materials while ignoring the in-depth comparison with related material systems.[26-36] Currently, the mechanisms of ML are still under intensive exploration due to the sophisticated factors involved in the process.[17, 32, 38, 42-48] The insufficient apprehending of ML mechanisms inevitably makes it difficult to guide the on-demand design of efficient ML materials. Therefore, in order to achieve the rational design and wide application of efficient ML materials, at the current stage, it is of pivotal significance to construct ML material platforms to achieve the systematical understanding of ML mechanisms.

In this work, we present a strategy of matrix microstructure evolution to construct ML material systems and dissect ML mechanisms (**Figure 1**). We demonstrate that through consecutive substitution of matrix skeleton cations in a series of ML material candidates, the crystal and electronic microstructures of material systems are comprehensively modulated, thereby individualizing the ML performance of each material (Figure 1a). This strategy not only enables the discovery of a batch of ML materials but also provides a well-connected platform for the multiscale experimental-theoretical explorations on the microscopic mechanism of achieving efficient ML performance.

2. Results and Discussion

As a proof-of-concept experiment, we started the microstructural evolution strategy by employing Mn^{2+}-activated Na_2ZnSiO_4 quaternary phosphor as the first model of ML material candidates (Figure 1b). This construction is based on comprehensive considerations, involving the screening scheme of ML materials, the sensitive d^5 electronic configuration of Mn^{2+} activators, as well as the physical and chemical stability of the material matrices. [37,49,50] Then,

we developed three A_2BMO_4-type matrices through sequentially replacing the matrix cations at the M, B and A sites considering valence balance and ionic size. Among the four matrix systems constructed, Na_2ZnSiO_4, Na_2ZnGeO_4 and Na_2MgGeO_4 have non-centrosymmetric structures with the space group $P1n1$ while Li_2ZnGeO_4 belongs to a centrosymmetric structure with the space group $P2_1/n$. Such a structural design aims to demonstrate the feasibility of both non-centrosymmetric and centrosymmetric structures in realizing the piezoluminescence, which breaks the limitation of non-centrosymmetric approaches reported previously. More importantly, these matrix systems are expected to provide evolutionary crystal and electronic microstructures for the activators to achieve distinctive ML performance and to systematically reveal the microstructure-luminescence relation.

Four Mn^{2+}-activated phosphor systems were prepared through solid-state chemistry among stoichiometric precursor metal oxides (Table S1, Supporting Information). Scanning electron microscopy (SEM) imaging displays that the size distribution of the as-synthesized crystal grains is in the range of 20–80 μm (Figure S1, Supporting Information). Rietveld refinement of X-ray diffraction (XRD) patterns reveals the formation of four target structures with high crystallinity (Figure S2 and Table S2, Supporting Information). The Mn^{2+} activators were found to preferentially enter the Zn^{2+}/Mg^{2+} sites and cause a slight expansion of four crystal lattices (Figure S3 and Table S3, Supporting Information). The fundamental ML evaluation demonstrates the optimal Mn^{2+} concentration to be Na_2ZnSiO_4:0.1mol%Mn^{2+} (Mn-NZSO), Na_2ZnGeO_4:0.1mol%Mn^{2+} (Mn-NZGO), Na_2MgGeO_4:0.1mol%Mn^{2+} (Mn-NMGO), and Li_2ZnGeO_4:0.25mol%Mn^{2+} (Mn-LZGO) (Figure S4, Supporting Information). Accordingly, we focused on these compositions in the following discussion.

We firstly investigated the optical properties of the four phosphor systems to confirm the validity of the matrix evolution strategy in regulating the microstructural environment of phosphors. The diffuse reflection spectra display the characteristic locations of the ultraviolet (UV) absorption edges in the four systems, indicating their difference in the optical bandgap (**Figure 2**a-d). The derived values of optical bandgap are in the order Mn-NZSO (5.61 eV) > Mn-NMGO (5.50 eV) > Mn-LZGO (5.27 eV) > Mn-NZGO (4.82 eV) (insets of Figure 2a−d). The introduction of Mn^{2+} dopants has a negligible effect on the optical bandgap of the four materials as confirmed by the characterizations (Figure S5, Supporting Information). Nevertheless, it significantly reduces the reflectance of the sample materials in the range of 200−800 nm due to the electromagnetic absorption of the Mn^{2+}-related energy levels and carrier traps. Based on an effective UV irradiation on phosphors (Figure S6, Supporting Information), the thermoluminescent (ThL) measurements were performed to investigate the variation of trap distribution. The ThL curves display a broad peak in the test range of 25−250 °C (Figure 2e−2h). It manifests the presence of traps in all Mn^{2+}-activated systems, which provides a prerequisite for the generation of trap-associated luminescence. The estimation of trap depth reveals the different depth distributions in the four material systems (insets of Figure 2e−h, Figure S7 and Table S4, Supporting Information). Accordingly, these Mn^{2+}-activated systems show persistent luminescence with different durations (Figure 2i). We observed a relatively longer duration of afterglow (AG) in Mn-NZSO (≥ 15 min, 0.63−0.77 eV) and Mn-LZGO (≥ 20 min, 0.66−0.92 eV) due to their deeper trap distributions. In contrast, Mn-NZGO (≥ 10 min, 0.63−0.68 eV) has a much shorter duration due to the shallowest trap distribution. The exception in Mn-NMGO (≥ 6 min, 0.66−0.76 eV) is probably due to the non-radiative relaxation process. To disclose the possible transfer process of electrons in traps, the dependence of reciprocal intensity on time is plotted based on the measured AG curves (Figure 2j). The linear fitting relation in Mn-NZSO, Mn-NMGO and Mn-LZGO reveals a tunneling process,[51] and the nonlinear relation in Mn-

NZGO will be discussed later. In addition, we noticed the diverse green-tone emission colors of the four Mn^{2+}-activated systems. These green-tone emissions including photoluminescence (PL), AG and ML are attributed to the $^4T_1(^4G)–^6A_1(^6S)$ transition of tetrahedrally coordinated Mn^{2+} ions.[52] These diverse colors arise from the spectral shift from Mn-NZSO (516 nm, grey-green) and Mn-NMGO (521 nm, green) to Mn-NZGO (524 nm, bright-green) and Mn-LZGO (530 nm, yellow-green) (Figure 2k, i), which is ascribed to the improvement of crystal-filed strength around Mn^{2+} activators (Figure 2m).[53]

We then evaluated the ML properties by incorporating these phosphors into an optically transparent epoxy resin elastomer. As expected, the four materials all show the ML responses to mechanical stress (**Figure 3**). Under the stimulation of cyclic friction, their ML signals show a period of oscillation that reacts synchronously to the switches and cycles of mechanical friction (Figure 3a−d). In these four systems, Mn-NZGO displays the highest signal-to-noise ratio due to the most intense ML signal and relatively weak AG noise (Figure 3b). Moreover, the ML signal of Mn-NZGO shows a relatively stable output under cyclic friction, which is comparable to the situation in the state-of-the-art ML materials $SrAl_2O_4:Eu^{2+}$ and $ZnS:Mn^{2+}$,[37] while is in sharp contrast to the continuous attenuation in conventional materials.[20,21,28] We also found that the strength of friction-triggered ML is not dependent on friction-rod materials including glass, polyethylene and metal.[54,55] Accordingly, the possibility of triboluminescence is ruled out.[37] We further executed a compression test on these ML materials to confirm the essence of piezoluminescence. It was found that the ML signals of four materials grew quantitatively with the increase of compressive load (Figure 3a), showing a typical characteristic of piezoluminescence.[29,37] Moreover, the ML intensity exhibits an increasing growth, in the order of Mn-NZGO > Mn-LZGO > Mn-NMGO > Mn-NZSO, which is consistent with that in the friction test. On the other hand, ML from the four systems shows a similar

recoverable property, revealing a trap-controlled ML process. Figure 3b, c display a representative recoverable ML from Mn-NZGO during the cyclic loading and UV irradiation. It is worth noting that the ML of Mn-NZGO exhibits outstanding high-sensitivity and slow-decay performance. First, the ML sensitively responds twice in each reciprocating cycle of compression-release deformation, and the peak intensity of ML during release even reaches 80% of that during compression. In contrast, most ML materials show only a weak or negligible response during the release process (Figure S8, Supporting Information). Second, after ten compression-release cycles, the ML intensity slowly attenuates by only less than 29%, which is significantly superior to the typical trap-controlled ML materials (Figure S8, Supporting Information). Such intense, sensitive and stable ML of Mn-NZGO ensures the potential application in the collection of dynamic ML photographs (Figure 3h) and real-time observation of stress concentration (Figure 3i and Figure S10, Supporting Information).

To investigate the relation of traps associated with AG and ML, we captured ML photographs of Mn-NZGO under different delays (Figure 3j) and plotted the decay trends of AG and ML by extracting the relative intensity (Figure 3k). These ML photographs intuitively show the gradual weakening of AG and ML, and the plotted trends further display that the attenuation of ML is much slower than that of AG. The ThL curves measured under different delays reveal that the evacuation of deep traps is significantly slower than that of shallow traps due to the higher activation energy required (Figure 3l and Figure S11, Supporting Information). We thus attributed the slow-attenuation behavior of ML relative to AG to the detrapping of deep traps due to higher activation energy available from mechanical stimulation than from ambient temperature.[37] It should be noted that there is no strict boundary between the deep and shallow traps due to their possible homology and connectivity.[12] In addition, the evaluation of the

luminescent intensity as a function of the activator concentration in the four systems shows that the critical Mn^{2+}concentration of the AG and ML processes is the same, but lower than that of the PL process (Figure S4, Supporting Information). This phenomenon is consistent with our previous report on Pr^{3+}-activated calcium niobates, which is ascribed to the trap-assisted long-distance energy transfer between adjacent luminescent activators.[42] We inferred reasonably that these results imply a common signature for the trap-controlled ML materials, which supplies significant guidance on the rational design of ML materials in future research.

Table 1 summarizes the structural symmetry, optical bandgap, trap distribution, and multi-luminescence properties of the four ML material systems developed in this work. In terms of structural symmetry, it shows that both non-centrosymmetric and centrosymmetric structures support the construction of trap-controlled piezoluminescence. The measurements of the piezoresponse force microscopy (PFM) on the individual particles reveal the local piezoelectric behaviors in the four material systems (Figure S12, Supporting Information), which further confirms the essence of piezoluminescence. Among the four material systems, Mn-NZGO exhibits the highest piezoelectricity. We inferred that the high piezoelectricity and rapid resilience of the crystal structure are the potential reasons for the high-sensitivity ML performance of Mn-NZGO. The piezoelectricity of Mn-LZGO with a centrosymmetric matrix may arise from the distortion of local symmetry caused by defects such as impurities and vacancies.[56] However, in terms of optical bandgap and trap distribution, their effects on the ML performance still seems to be complicated and unclear. It is of importance to note that the strongest ML does not appear in the materials with the highest trap concentration (Mn-NZSO) or the deepest depth (Mn-LZGO). This phenomenon is inconsistent with our previous understandings,[37] which implies the complexity of carrier transport in the current ML system.

To reveal the roles of optical bandgap and trap distribution in promoting ML performance, we investigated the electronic structure variation of four material systems by the density functional theory (DFT). Although these four systems share the same stoichiometry, their lattice structures are different. From the real spatial 3D orbital contour plots, the active bonding and antibonding orbitals near the Fermi level (E_F) are noticed near the Si and O sites in NZSO (**Figure 4**a). Similarly, we have noticed that all the electroactive regions are dominated by Ge and O sites in NZGO, NMGO and LZGO (Figure 4b−d). We have further looked into the electronic structures regarding the projected partial density of states (PDOS). In NZSO, the p-orbitals are the main contribution to the valence band maximum (VBM) and conduction band minimum (CBM), indicating their essential role in the modulation of ML performance (Figure 4e). Such dominant occupation of p-orbitals is also noticed in NZGO, NMGO and LZGO. In contrast, the d-orbitals of Zn locate at a deep position of E_V-4.0 eV (E_V = 0 eV), which shows limited modulation to the electron transfer. Meanwhile, the well-overlapped s-p couplings exist in all four systems. From the PDOS, the bandgap size of the four material systems is revealed in the order NZSO > NMGO > LZGO > NZGO. In particular, the NZSO, NMGO and LZGO show very close bandgap while the bandgap of NZGO is evidently smaller, which are consistent with the experimental results (Figure 4e−h).

Since the Mn^{2+} dopant shows a limited influence on the bandgap, we need to further demonstrate their effect from the changes in local electronic structure. For the s-orbitals, we noticed the consistent band offset of the VBM and CBM, accompanied by the appearance of gap states close to E_F. These gap states are able to alleviate the electron transfer efficiency to achieve high-performance ML (Figure 4i). We have considered the p-orbital contribution from

two different sites including Ge/Si and O sites for these four materials. For the p-orbitals of O sites, the band offset of VBM is observed with the formation of two electronic states within the bandgap, which also significantly promotes the electron transfer (Figure 4j). For the p-orbitals of Ge and Si sites, the doped Mn^{2+} activators lead to the formation of trap states below the CBM, in which the Mn-NZGO shows the shallowest trap states. The shallow trap states allow the electron transfer for the ML process through both tunneling and the conduction band (Figure 4k). For the Mn^{2+} dopants, the d-orbitals of nearby Zn sites only demonstrate the VBM band offset of 1.57 eV without the formation of any gap states, further confirming the key role of p-electrons for achieving ML rather than d-electrons (Figure 4l). The Mn^{2+} dopants reflect similar d-band occupations in all four materials, which has a negligible effect on the bandgap as the experimental results (Figure 4m). In the end, we summarized the Mn^{2+} doping induced gap states for realizing the ML in four different systems. With the formation of the inter-electronic-levels, the barriers for the electronic excitation and transition barrier from VB to CB has been evidently lowered. In particular, due to the shallowest trap depth of Mn-NZGO, the additional electron transfer pathway for ML through the CB is also possible, supporting the experimental results (inset of Figure 2j). Meanwhile, direct tunneling from these inter-electronic-levels to Mn^{2+} levels is also enabled. Thus, the efficiency of electron-hole recombination for the ML is also significantly promoted by the band offset induced by Mn^{2+} doping, which further transfers the energy to excite the electrons of Mn^{2+} to achieve the efficient ML (Figure 4n). For the Mn^{2+} doping in four different systems, the NMGO shows the highest energy cost of 2.61 eV, which is much larger than the other three materials due to the stronger *s-p* couplings of Mg-O bond than *p-d* couplings of Zn-O bonds in the other three compounds. NZSO and NZGO show a similar energy cost of 0.29 and 0.31 eV for the Mn doping, respectively. The formation energy of Mn-LZGO is 0.41 eV (Figure 4o). Therefore, theoretical calculations have confirmed the local electronic environment changes induced by the introduction of Mn^{2+} dopants, which not

only lowers the barriers to accelerate electron transfer but also supplies electron trap states to promote the ML performance.

Inspired by the individualized multi-luminescence of the four material systems, we have designed a multidimensional anti-counterfeiting application that involves multicolor emissions, diverse AG durations, and unique ML displays. **Figure 5**a presents a typical fabrication procedure of leaf-shaped composite films, including the separate mixing of four phosphors and an optically transparent epoxy resin, slurries filling in pattern grooves, and thermoforming. Figure 5b presents the optical image of the prepared leaf-shaped composite film under natural light. Figure 5c illustrates the triple-modal (PL, AG and ML), four-color and multi-duration luminescence for multidimensional anti-counterfeiting. When excited by a handheld 254 nm UV lamp, four green-tone luminescent leaves can be clearly observed in a dark room. After turning off the UV irradiation, the four leaves further exhibit significantly different AG durations. By using a pen to write on the irradiated pattern, we can further observe the differentiated ML displays from the four leaves. More intriguing, the brightest ML display was observed in the leaf II ($Na_2ZnGeO_4:Mn^{2+}$) with a relatively weak AG, rather than in the leaf IV ($Li_2ZnGeO_4:Mn^{2+}$) with the strongest persistent luminescence. These multidimensional displays based on four evolutionary material systems provide unique authentication information for anti-counterfeiting applications and other flexible detections. The unique luminescence performance is beyond the traditional cognition, enabling high-level information security. In addition, the light emission of the composite pattern has excellent water-resistance stability due to the water-proof ability of the materials (Figure S13, Supporting Information) and the extra protection of epoxy resin, showing the usability in a humid environment (Figure 5d).

3. Conclusion

In summary, we have demonstrated a facile strategy of matrix microstructure evolution, which enables the systematic modulation of the crystal and electronic microstructures of material systems, thereby providing a well-connected platform between discovering ML materials and dissecting ML mechanisms. The effectiveness of the strategy has been confirmed by constructing and evaluating a series of Mn^{2+}-activated $(Na/Li)_2(Zn/Mg)(Si/Ge)O_4$ systems. Among them, $Na_2ZnGeO_4:Mn^{2+}$ shows the superior ML performance of intense brightness, high mechanical sensitivity, and excellent stability and repeatability, which are particularly suitable for visual observation of stress distribution. Through systematic experimental investigations and theoretical analysis, the main factors for developing and improving ML have been revealed. First, the construction of piezoluminescence overcomes the previous limitations of non-centrosymmetric matrices. Second, the inter-electronic-levels and shallow electron traps induced by activator doping facilitate the electron recombination efficiency through both tunneling and conduction band transfer mechanisms. Third, compared with photoluminescence, the critical concentration of the activators in ML is lower due to the trap-assisted energy transfer process. In addition, by combing the distinctive multi-luminescence of the four materials developed, we have successfully designed and fabricated a multidimensional smart anti-counterfeiting application based on the reported materials. Our work sheds the light on the rapid exploitation of ML material systems and a comprehensive understanding of ML mechanisms as well as the underlying structure-activity relationship. This work opens up a new avenue in ML to achieve efficient screening and design of potential ML materials, which will benefit the future research of ML materials for the wide application in different fields.

Supporting Information

Supporting Information is available from the Wiley Online Library or from the author.

Acknowledgements

This work was supported by the National Natural Science Foundation of China (11774189 and 51772270, 21771156), the National Key R&D Program of China (2018YFB1107200), the Basic Scientific Fund for National Public Research Institutes of China (2018Y02) and the Early Career Scheme (ECS) fund (PolyU 253026/16P) from the Research Grant Council (RGC) in Hong Kong.

Received: ((will be filled in by the editorial staff))
Revised: ((will be filled in by the editorial staff))
Published online: ((will be filled in by the editorial staff))

References

[1] Z. L. Wang, *Nature* **2017**, *542,* 159.

[2] Z. L. Wang, J. Song, *Science* **2006**, *312,* 242.

[3] M. Dukic, M. Winhold, C. H. Schwalb, J. D. Adams, V. Stavrov, M. Huth, G. E. Fantner, *Nat. Commun*. **2016**, *7*, 12487.

[4] S. Z. Guo, K. Qiu, F. Meng, S. H. Park, M. C. McAlpine, *Adv. Mater*. **2017**, *29*, 1701218.

[5] J. Hao, C. N. Xu, *MRS Bull.* **2018**, *43*, 965.

[6] C. Wang, Y. Yu, Y. Yuan, C. Ren, Q. Liao, J. Wang, Z. Chai, Q. Li, Z. Li, *Matter* **2020**, *2*, 181.

[7] B. Yin, X. Liu, H. Gao, T. Fu, J. Yao, *Nat. Commun.* **2018**, *9*, 5161.

[8] Y. Shi, B. Polat, Q. Huang, D. J. Sirbuly, *Nat. Protoc*. **2018**, *13*, 2714.

[9] M. T. Chorsi, E. J. Curry, H. T. Chorsi, R. Das, J. Baroody, P. K. Purohit, H. Ilies, T. D. Nguyen, *Adv. Mater*. **2019**, *31,* 1802084.

[10] J. S. Kim, Y. N. Kwon, N. Shin, K. S. Sohn, *Appl. Phys. Lett*. **2007**, *90*, 241916.

[11] L. Liu, C. N. Xu, A. Yoshida, D. Tu, N. Ueno, S. Kainuma, *Adv. Mater. Technol*. **2019**, *4*, 1800336.

[12] J. C. Zhang, X. H. Fan, X. Yan, F. Xia, W. Kong, Y. Z. Long, X. Wang, *Acta Mater*. **2018**, *152*, 148.

[13] S. M. Jeong, S. Song, S. K. Lee, N. Y. Ha, *Adv. Mater.* **2013**, *25*, 6194.

[14] S. M. Jeong, S. Song, K. I. Joo, J. Kim, S. H. Hwang, J. Jeong, H. Kim, *Energy Environ. Sci*. **2014**, *7*, 3338.

[15] S. M. Jeong, S. Song, H. J. Seo, W. M.Choi, S. H. Hwang, S. G. Lee, S. K. Lim, *Adv. Sustain. Syst*. **2017**, *1*, 1700126.

[16] M. C. Wong, L. Chen, M. K. Tsang, Y. Zhang, J. Hao, *Adv. Mater*. **2015**, *27*, 4488.

[17] M. C. Wong, L. Chen, G. Bai, L. B. Huang, J. Hao, *Adv. Mater*. **2017**, *29*, 1701945.

[18] D. Tu, C. N. Xu, S. Kamimura, Y. Horibe, H. Oshiro, L. Zhang, Y. Ishii, K. Hyodo, G. Marriott, N. Ueno, X. G. Zheng, *Adv. Mater*. **2020**, *32*, 1908083.

[19] X. Wang, H. Zhang, R. Yu, L. Dong, D. Peng, A. Zhang, Y. Zhang, H. Liu, C. Pan, Z. L. Wang, *Adv. Mater*. **2015**, *27*,2324.

[20] J. C. Zhang, C. Pan, Y. F. Zhu, L. Z. Zhao, H. W. He, X. Liu, J. Qiu, *Adv. Mater*. **2018**, *30*, 1804644.

[21] T. Jiang, Y. F. Zhu, J. C. Zhang, J. Zhu, M. Zhang, J. Qiu, *Adv. Funct. Mater.* **2019**, *29*, 1906068.

[22] Z. Ma, J. Zhou, J. Zhang, S. Zeng, H. Zhou, A. T. Smith, W. Wang, L. Sun, Z. Wang, *Mater. Horiz*. **2019**, *6*, 2003.

[23] X. Qian, Z. Cai, M. Su, F. Li, W. Fang, Y. Li, X. Zhou, Q. Li, X. Feng, W. Li, X. Hu, X. Wang, C. Pan, Y. Song, *Adv. Mater*. **2018**, *30*, 1800291.

[24] D. K. Patel, B. E. Cohen, L. Etgar, S. Magdassi, *Mater. Horiz.* **2018**, *5*, 708.

[25] R. R. Petit, S. E. Michels, A. Feng, P. F. Smet, *Light Sci. Appl*. **2019**, *8*, 124.

[26] C. N. Xu, T. Watanabe, M. Akiyama, X. G. Zheng, *Appl. Phys. Lett*. **1999**, *74*, 2414.

[27] C. N. Xu, T. Watanabe, M. Akiyama, X. G. Zheng, *Appl. Phys. Lett*. **1999**, *74*, 1236.

[28] J. C. Zhang, C. N. Xu, S. Kamimura, Y. Terasawa, H. Yamada, X. Wang, *Opt. Express* **2013**, *21*, 12976.

[29] D. Tu, C. N. Xu, A. Yoshida, M. Fujihala, J. Hirotsu, X. G. Zheng, *Adv. Mater*. **2017**, *29*, 1606914.

[30] J. C. Zhang, L. Z. Zhao, Y. Z. Long, H. D. Zhang, B. Sun, W. P. Han, X. Yan, X. Wang, *Chem. Mater*. **2015**, *27*, 7481.

[31] L. Li, L. Wondraczek, M. Peng, Z. Ma, B. Zou, *Nano Energy.* **2020**, *69,* 104413.

[32] C. Chen, Y. Zhuang, D. Tu, X. Wang, C. Pan, R. J. Xie, *Nano Energy* **2020**, *68*, 104329.

[33] D. Peng, Y. Jiang, B. Huang, Y. Du, J. Zhao, X. Zhang, R. Ma, S. Golovynskyi, B. Chen, F. Wang, *Adv. Mater*. **2020**, *32*, 1907747.

[34] Y. Du, Y. Jiang, T. Sun, J. Zhao, B. Huang, D. Peng, F. Wang, *Adv. Mater*. **2019**, *31*, 1807062.

[35] J. Zhou, Y. Gu, J. Lu, L. Xu, J. Zhang, D. Wang, W. Wang, *Chem. Eng. J.* **2020**, *390*, 124473.

[36] A. Feng, P. F. Smet, *Materials* **2018**, *11*, 484.

[37] J. C. Zhang, X. Wang, G. Marriott, C. N. Xu, *Prog. Mater. Sci.* **2019**, *103*, 678.

[38] J. Botterman, K. V. D. Eeckhout, I. D. Baere, D. Poelman, P. F. Smet, *Acta Mater*. **2012**, *60*, 5494.

[39] S. Kamimura, H. Yamada, C. N. Xu, *Appl. Phys. Lett.* **2012**, *101*, 091113.

[40] X. H. Fan, J. C. Zhang, M. Zhang, C. Pan, X. Yan, W. P. Han, H. D. Zhang, X. Wang, *Opt. Express* **2017**, *25,* 14238.

[41] J. C. Zhang, Y. Z. Long, X. Yan, X. Wang, F. Wang, *Chem. Mater.* **2016**, *28,* 4052.

[42] A. Feng, S. Michels, A. Lamberti, W. V. Paepegem, P. F. Smet, *Acta Mater*. **2020**, *183*, 493.

[43] H. Chen, L. Wu, T. Sun, R. Dong, Z. Zheng, Y. Kong, Y. Zhang, J. Xu, *Appl. Phys. Lett.* **2020**, *116*, 051904.

[44] D. Tu, C. N. Xu, Y. Fujio, A. Yoshida, *Light Sci. Appl.*, **2015**, 4, e356.

[45] Y. Zhuang, D. Tu, C. Chen, L. Wang, H. Zhang, H. Xue, C. Yuan, G. Chen, C. Pan, L. Dai, R. J. Xie, *Light Sci. Appl.*, **2020**, 9, 182.

[46] Y. Zhou, Y. L. Yang, Y. T. Fan, W. Yang, W. B. Zhang, J. F. Hu, Z. J. Zhang, J. T. Zhao, *J. Mater. Chem. C*, **2019**, 7, 8070.

[47] B. Huang, *Phys. Chem. Chem. Phys.*, **2016**, 18, 25946.

[48] B. Huang, M. Sun, D. Peng, *Nano Energy*, **2018**, 47, 150.

[49] Y. Li, M. Gecevicius, J. Qiu, *Chem. Soc. Rev.* **2016**, *45*, 2090.

[50] H. Chen, L. Wu, F. Bo, J. Jian, L. Wu, H. Zhang, L. Zheng, Y. Kong, Y. Zhang, J. Xu, *J. Mater. Chem. C.* **2019**, *7*, 7096

[51] Z. Pan, Y. Y. Lu, F. Liu, *Nat. Mater*. **2012**, *11*, 58.

[52] C. J. Duan, A. C. A. Delsing, H. T. Hintzen, *Chem. Mater*. **2009**, *21*, 1010.

[53] I. Hernández, F. Rodríguez, H. D. Hochheimer, *Phys. Rev. Lett.* **2007**, *99*, 027403.

[54] Z. L. Wang, *ACS Nano.* **2013**, *7*, 9533.

[55] H. Matsui, C. N. Xu, Y. Liu, H. Tateyama, *Phys. Rev. B* **2004***, 69*, 235109.

[56] M. Alexe, A. Gruvermann, Nanoscale Characterization of Ferroelectric Materials–Scanning Probe Microscopy Approach, Springer, Berlin **2004**.

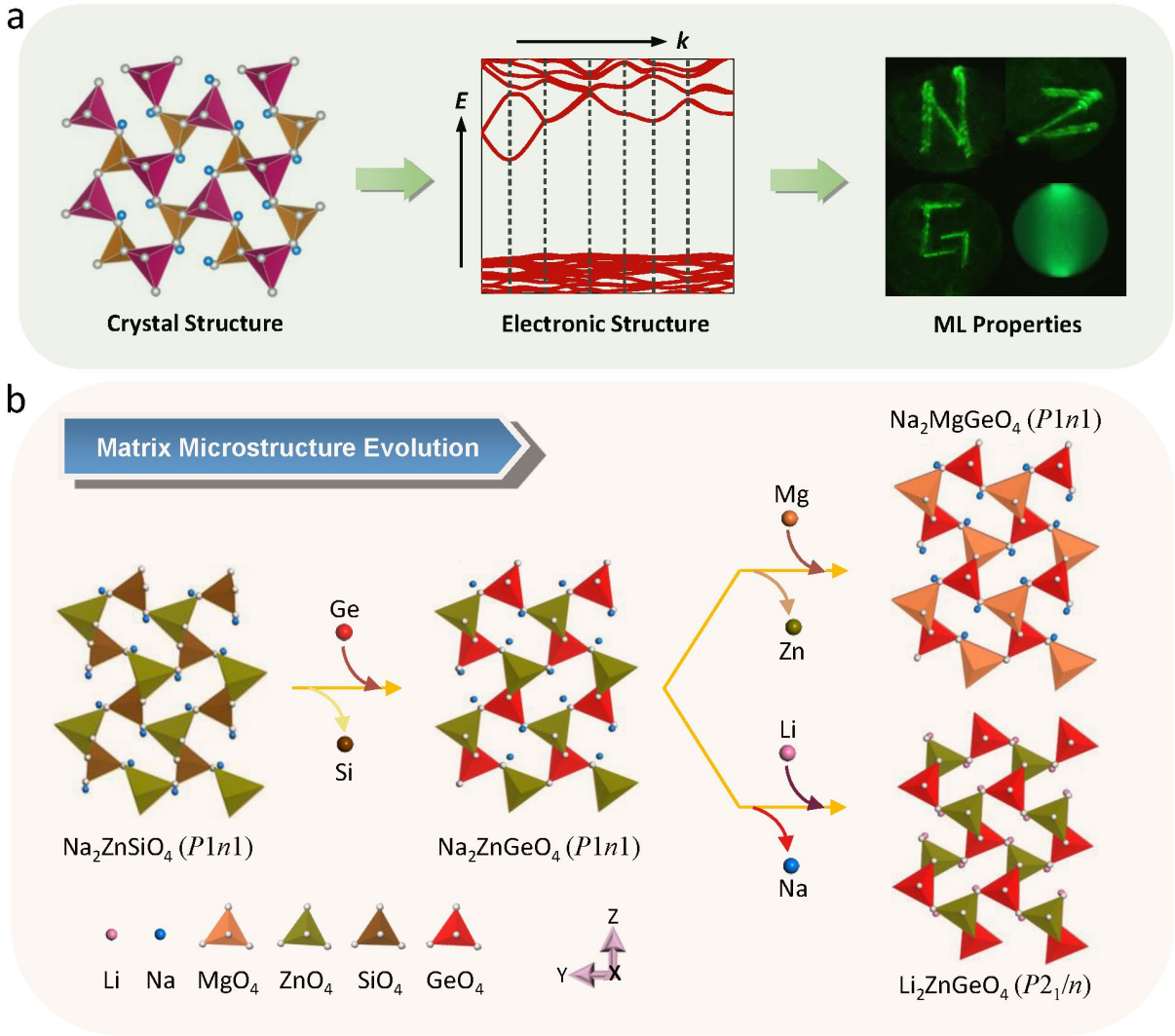

Figure 1. Strategy for matrix microstructure evolution. (a) Schematic diagram of the causal correlation between crystal structure, electronic structure and ML properties. (b) Structural illustration of the rational design of four quaternary crystal matrices by replacing skeleton cations.

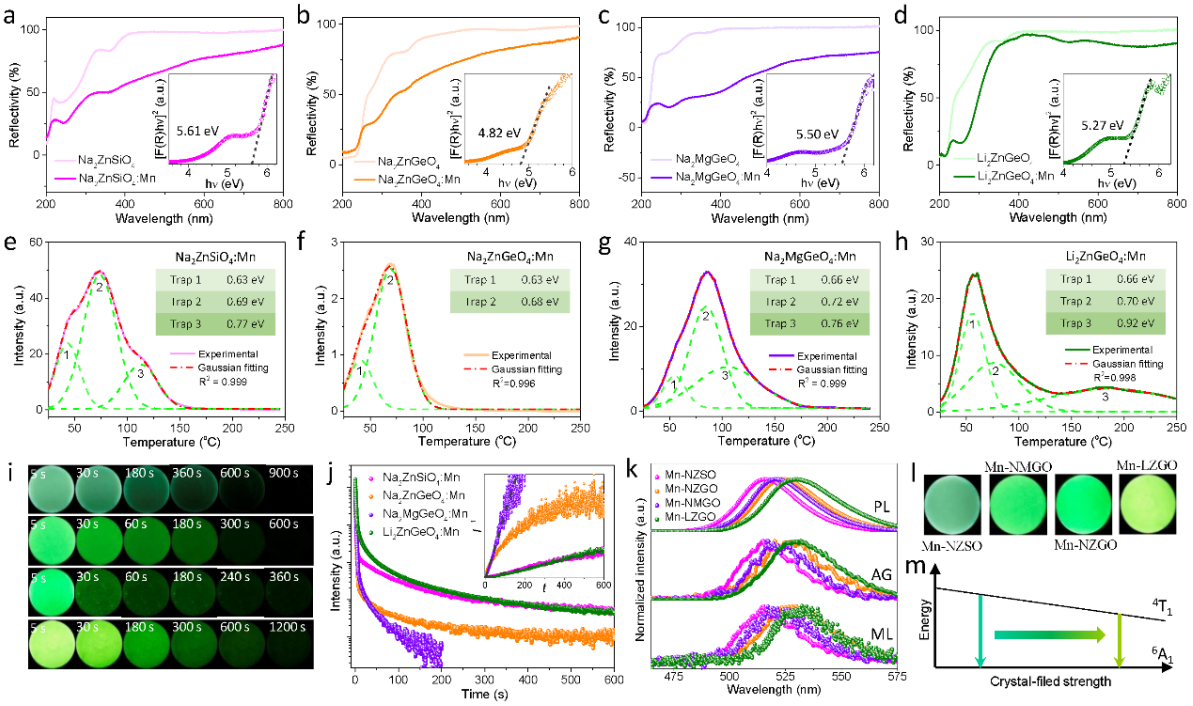

Figure 2. Optical properties of $Na_2ZnSiO_4:Mn^{2+}$, $Na_2ZnGeO_4:Mn^{2+}$, $Na_2MgGeO_4:Mn^{2+}$ and $Li_2ZnGeO_4:Mn^{2+}$ phosphors. (a–d) Diffuse reflectance spectra of four materials before and after doping with Mn^{2+} activators. The insets show the derivation of the optical bandgap. (e–h) ThL curves and related Gaussian deconvolution. The insets list the estimated depths of traps. (i) AG photographs captured under different delays (top to bottom: $Na_2ZnSiO_4:Mn^{2+}$, $Na_2ZnGeO_4:Mn^{2+}$, $Na_2MgGeO_4:Mn^{2+}$ and $Li_2ZnGeO_4:Mn^{2+}$). (j) Decay curves of AG by monitoring the $^4T_1(^4G)$–$^6A_1(^6S)$ transition of Mn^{2+} activators. The inset shows the AG intensity (I^{-1}) as a function of time (t). (k) Normalized spectra of PL, AG and ML. (I) PL photographs. (m) Schematic illustration of the spectral shift caused by the crystal-field strength.

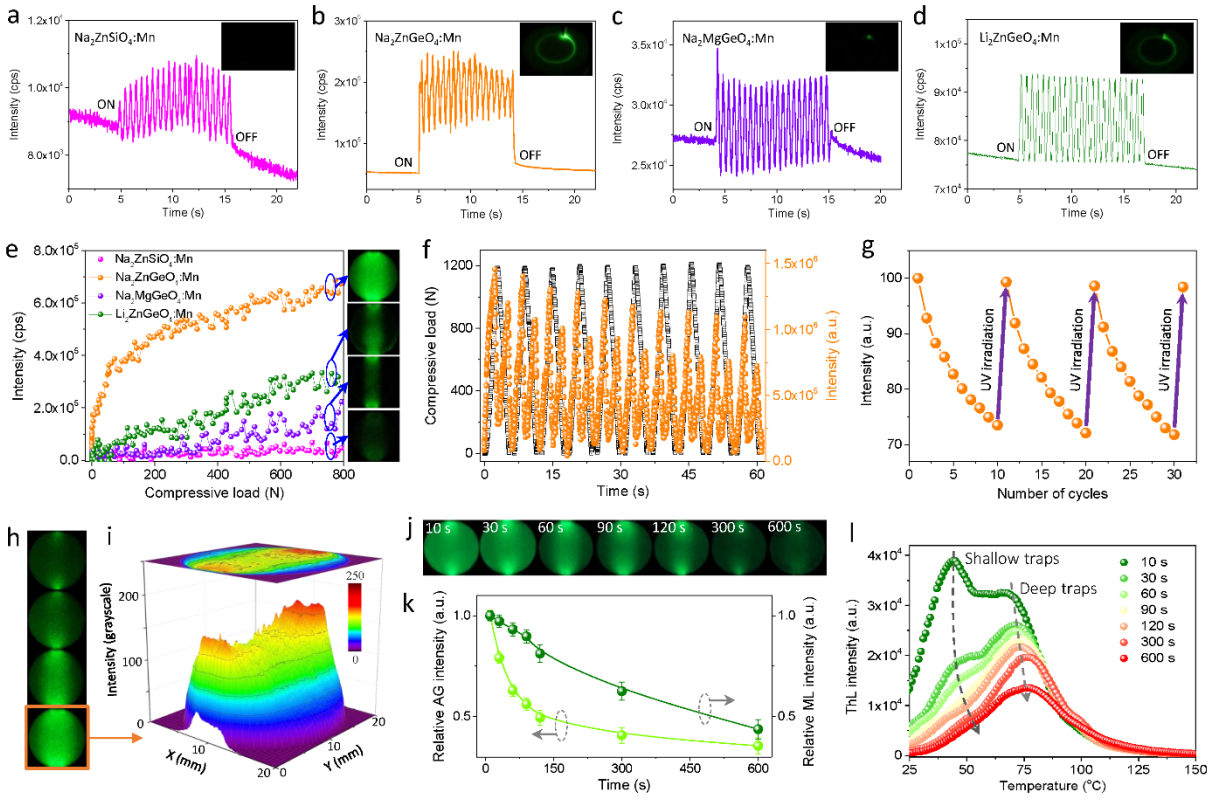

Figure 3. Trap-controlled ML of $Na_2ZnSiO_4:Mn^{2+}$, $Na_2ZnGeO_4:Mn^{2+}$, $Na_2MgGeO_4:Mn^{2+}$ and $Li_2ZnGeO_4:Mn^{2+}$ phosphors. (a−d) ML responses of four samples on cyclic friction (5 MPa, 2 round s^{-1}). The insets show the photographs of friction-triggered ML. (e) ML responses of four samples on mechanical compression (0−800 N, 3 mm min^{-1}). The insets show the photographs of compression-triggered ML. (f) ML curve of $Na_2ZnGeO_4:Mn^{2+}$ under cyclic compression (0−1200 N, 10 mm min^{-1}), exhibiting high-sensitive and slow-decay ML. (g) ML reproducibility of $Na_2ZnGeO_4:Mn^{2+}$ under cyclic loading and UV irradiation. (h) Dynamic ML photographs of $Na_2ZnGeO_4:Mn^{2+}$ under different compression loads (top to bottom: 100, 300, 500 and 800 N; 3 mm min^{-1}). (i) Grayscale distribution extracted from a dynamic ML photograph. (j) Compression-triggered ML photographs of $Na_2ZnGeO_4:Mn^{2+}$ captured under different delays (10−600 s). (k) Dependence of relative AG and ML intensity on time extracted from (j). (l) ThL curves measured under different delays (10−600 s).

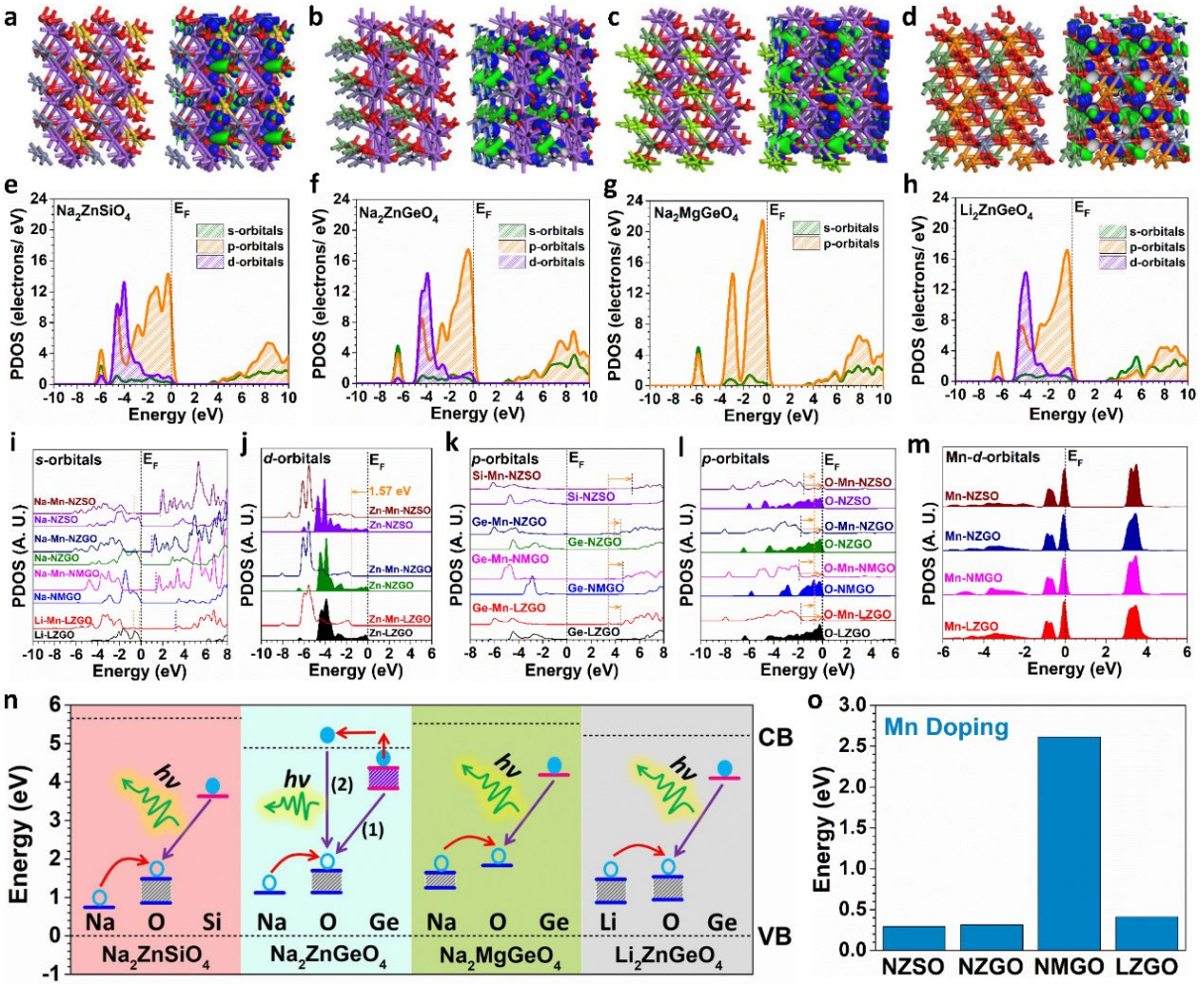

Figure 4. Theoretical calculations for four ML material systems. (a–d) The real spatial 3D orbital contour plots for (a) $NaZnSiO_4$, (b) $NaZnGeO_4$, (c) $NaMgGeO_4$, and (d) $LiZnGeO_4$. (e–h) The PDOSs of (e) $NaZnSiO_4$, (f) $NaZnGeO_4$, (g) $NaMgGeO_4$, and (h) $LiZnGeO_4$. (i) The s-orbitals band offset of Na/Li sites in four different material systems induced by Mn^{2+} dopants. (j) The d-orbitals band offset of Zn sites in three different material systems induced by Mn^{2+} dopants. (k) The p-orbitals band offset of Ge/Si sites in four different material systems induced by Mn^{2+} dopants. (l) The p-orbitals band offset of O sites in four different material systems induced by Mn^{2+} dopants. (m) The PDOSs of Mn^{2+} dopants in four different material systems. (n) The summarized electron-transfer-and-recombination pathways for Mn^{2+}-activated $NaZnSiO_4$, $NaZnGeO_4$, $NaMgGeO_4$, and $LiZnGeO_4$. (o) The energy cost of Mn^{2+} doping in four different material systems.

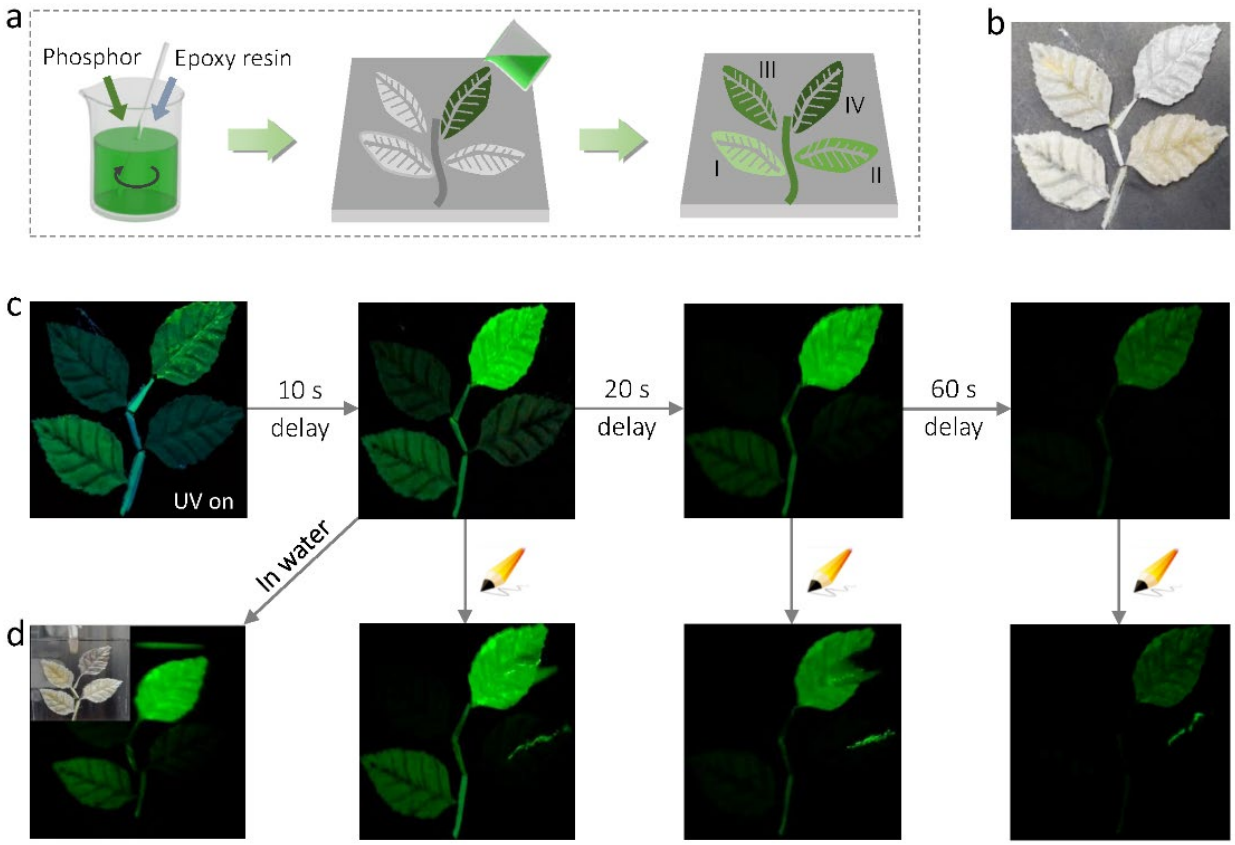

Figure 5. Preparation of patterned composite films and demonstration of multidimensional anti-counterfeiting. (a) Fabrication procedure of the leaf patterns consisting of four phosphors (I. $Na_2ZnSiO_4:Mn^{2+}$, II. $Na_2ZnGeO_4:Mn^{2+}$, III. $Na_2MgGeO_4:Mn^{2+}$ and IV. $Li_2ZnGeO_4:Mn^{2+}$) embedded in the epoxy resin elastomer. (b) Photograph of the leaf-shaped composite film under natural light. (c) Illustration of triple-modal (PL, AG and ML), four-color and multi-duration luminescence for multidimensional anti-counterfeiting. The UV irradiation is 254 nm for 10 s. (d) Luminous stability of leaf-shaped composite film against water immersion.

Table 1. Summarization of the structural symmetry, optical bandgap, trap distribution, and multi-luminescence properties of four ML material systems developed in this work. Trap density*: Relative value, which is equivalently derived from the relative ThL integral intensity. ML intensity#: Relative intensity.

Materials	Space group	Host symmetry	Bandgap	Optical transition	Emission peak (color)	Trap density *	Trap depth	Afterglow duration	ML intensity #
$Na_2ZnSiO_4:Mn^{2+}$	*P*1*n*1 (no.7)	×	5.6 eV	$^4T_1-^6A_1$	516 nm (grey-green)	100	0.63–0.77 eV	≥ 15 min	7
$Na_2ZnGeO_4:Mn^{2+}$	*P*1*n*1 (no.7)	×	4.86 eV	$^4T_1-^6A_1$	524 nm (bright-green)	4	0.63–0.68 eV	≥ 10 min	100
$Na_2MgGeO_4:Mn^{2+}$	*P*1*n*1 (no.7)	×	5.50 eV	$^4T_1-^6A_1$	521 nm (green)	63	0.66–0.76 eV	≥ 6 min	35
$Li_2ZnGeO_4:Mn^{2+}$	$P2_1/n$ (no.14)	○	5.21 eV	$^4T_1-^6A_1$	530 nm (yellow-green)	48	0.66–0.92 eV	≥ 20 min	50